Materials & Design 210 (2021) 110085

Contents lists available at ScienceDirect

Materials & Design

journal homepage: www.elsevier.com/locate/matdes

Effect of water atomization on properties of type 4130 steel processed by L-PBF

M. Abdelwahed [a,b,*], S. Bengtsson [c], R. Casati [a], A. Larsson [c], S. Petrella [d], M. Vedani [a]

[a] Politecnico di Milano, Department of Mechanical Engineering, 20156 Milan, Italy
[b] Department of Design and Production Engineering, Faculty of Engineering, Ain Shams University, 11517 Cairo, Egypt
[c] Höganäs AB, 26383 Höganäs, Sweden
[d] Certema, 58044 Cinigiano, GR, Italy

HIGHLIGHTS

- Laser Powder Bed Fusion processed 4130 steels starting from gas and water atomized powders have been studied.
- Oxide-based inclusions were found within the water atomized steel matrix that activate the ductile fracture during tensile testing.
- Micro-segregation of alloying elements was detected during the laser-processing of both steels, which contributed to a local increase in microhardness.
- Water atomized steel deliver comparable mechanical properties to counterparts processed from gas atomized powder after tuning the post-process thermal treatment.

GRAPHICAL ABSTRACT

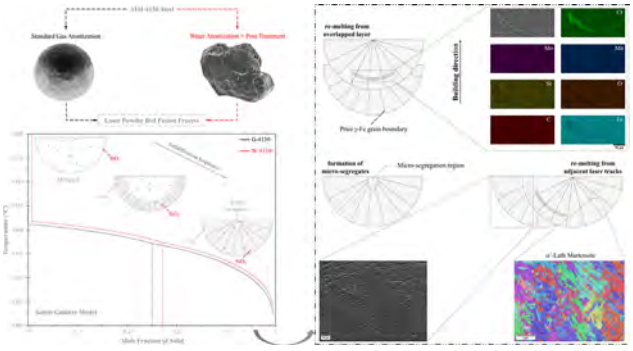

ARTICLE INFO

Article history:
Received 28 June 2021
Revised 6 August 2021
Accepted 2 September 2021
Available online 04 September 2021

Keywords:
Laser Powder Bed Fusion
Water Atomized Powder
Low-Alloy Steel
Micro-segregation
EBSD
Mechanical behavior

ABSTRACT

In the current investigation, a comparison between two type 4130 low-alloy steel powders produced by both gas and water atomization, and later processed by Laser-powder bed fusion was carried out. Samples fabricated from the water atomized powder showed relative density levels exceeding 99%, slightly lower than those achieved with the gas atomized powder. Both steels exhibited similar metallurgical features after solidification, showing a microstructure that is mainly composed of partially tempered martensite, bainite, and retained austenite. Additionally, micro-segregation of alloying elements was detected in the as-built microstructure, which contribute to a local increase in microhardness. The excess of oxygen found in the water atomized powder tended to combine with silicon and form nano-sized SiO_2 inclusions. During the laser processing, the complex heating and cooling effects generated by adjacent laser tracks and by overlapping layers led to an in-situ tempering of the fresh martensite. Accordingly, the hardness values of steels in as-built condition were equivalent to those of conventionally quenched samples tempered at 350 °C and 450 °C, for gas atomized and water atomized steels, respectively. Finally, a comparison in terms of mechanical properties of the investigated steels showed that the powder atomization process resulted in limited changes in steel performance.

* Corresponding author.
E-mail addresses: marawan.abdelwahed@polimi.it, marwan.faisal@eng.asu.edu.eg (M. Abdelwahed).

https://doi.org/10.1016/j.matdes.2021.110085
0264-1275/

1. Introduction

Laser-Powder Bed Fusion (L-PBF) is considered as the main processing technology for additive manufactured (AM) of metal components. The remarkable ability of L-PBF to consolidate powders layer-by-layer allows to design objects with high degree of freedom and complexity, with minimal material wastes. The reference materials for L-PBF process are aluminum, titanium, steels and nickel-based superalloys [1,2] for most of the structural applications in aerospace, machinery, transportation and biomedical fields.

Despite the widespread and predominant applications of steels for structural parts produced by conventional routes due to low cost, optimal processability and large variety of grades available, the use of Fe-based alloys in L-PBF has not reached the same degree of confidence yet. Indeed, even if stainless steels and maraging grades have been extensively investigated in the literature [3–11] and are always found within the materials library of L-PBF system producers, a relatively limited number of studies have been performed up to now on plain-carbon and low-alloy AM steels for structural applications [12–19]. For the definition of the solidification microstructure and defect generation in L-PBF-processed alloys, reference is often made to welding metallurgy principles due to similar mechanisms for the growth of solid phase from liquid melt and comparably fast cooling conditions [1]. Consistently, one of the main concerns for the successful L-PBF processing of alloyed steels is the mitigation of hot- and cold cracking defects that are easily generated in steels with high carbon equivalent number [14]. Wang and Kelly [14] were able to suppress the welding defects in a L-PBF processed 4140 steel by using a pre-heated substrate. In another work performed on the same grade, Damon and co-workers [15] demonstrated the intrinsic tempering phenomena taking place during the laser processing. These authors showed that the mechanical performance of the as-built microstructure was comparable to that of the cast alloy subjected to quenching and a 450 °C tempering treatment. The same result was also achieved by Abdelwahed et al. on several plain-carbon and low-alloyed steels [20]. Han and co-workers stated that after solidification, depending on the initial temperature of the substrate as well as on the L-PBF processing parameters, the as-built microstructure of a 24CrNiMo steel was composed of variable amounts of fresh martensite, retained austenite, upper and lower bainite, and tempered martensite along with precipitated carbides [16]. It was also shown that the microstructural constituents could vary in amount and type at different positions of the build height due to the different thermal histories experienced. Dilip and co-authors [17] processed a HY100 steel by L-PBF. Their microstructural analyses revealed an epitaxial growth of the prior austenitic grains in the building direction, leading to orientation-related mechanical properties. The findings also demonstrated that the application of conventional quench and tempering treatments on laser-processed steel suppress the anisotropic effects [17,18].

The high cost of products is one of the main drawbacks of the L-PBF technology in many industries relying on mass-production scale. Hence, the product cost optimization is a challenging topic. In an expenditure-assessment of automotive parts produced by additive manufacturing (AM), Lindemann et.al [21] demonstrated that the AM machine depreciation contributes to the major cost of the final product followed by the feedstock powder which represents around 11% of the share. So far, gas atomization (GA) processes have been widely used to produce feedstock powder especially for the L-PBF technology, due to the ability to produce spherical particles with close control of composition, through a fairly expensive process, which becomes inefficient especially for large production batches. On the contrary, water atomization (WA) takes advantage of the high production rates and lower consumable costs, thus representing an alternative way for a cheaper and more sustainable powder production route [22]. Limited studies have been carried out in the literature on the L-PBF or other processing techniques of WA powders. Among these, investigations have been carried out on iron [23,24], 316L [25–27] and 17-4PH [28–30] stainless steels, as well as on few low-alloyed steels [20]. These papers highlighted the possibility to consolidate the WA powders, achieving high density and good mechanical properties compared to counterparts fabricated from GA powders.

The WA process requires some modification in the steel chemistry to adapt to the higher activity of oxygen generally found upon powder processing. In that sense, oxidizing elements such as manganese and aluminum are not any longer favored in WA steel powders [31]. In a previous study carried out by the present authors [20] on L-PBF processing of WA steels, it was highlighted that micrometer- or submicrometer-sized $MnO\text{-}SiO_2$ inclusions exist in Mn-bearing steels. In addition, more complex multiphase oxides of the type $Cr_2O_3\text{-}SiO_2$ could form when chromium level exceeds 3 wt% in alloy-steels. The oxide-based inclusions did not show a significant effect on the tensile performance of the investigated steels and played a role by activating micrometric- and submicrometric dimples according to the ductile fracture mechanism. However, it is known that micro-voids initiated by the oxide-based inclusions can reduce the impact toughness in L-PBF GA-316L stainless steel, as demonstrated by Lou et. al. [32].

In this research, a comparison between a type 4130 GA powder steel and a modified version of it produced by WA is presented. The two feedstock powders were processed by L-PBF and the effect of powder formulation on the metallurgical features, post-process thermal treatment response, as well as resulting mechanical properties are addressed.

2. Material and experimental procedures

2.1. Feedstock powder and L-PBF process

In the current investigation, powders based on the AISI 4130 steel (equivalent to 25CrMo4 and 1.7218 grades for the European standards) have been produced by GA as a standard powder production route and by WA as an alternative route. The chemical composition of the investigated powders, supplied by Höganäs AB, is given in Table 1.

A proprietary mechanical treatment was later applied to the WA powder to modify the powder particles surface and consequently enhance the powder characteristics. The particle size distribution of the 4130 powders was verified according to ISO 4497 Sieve Analysis standard and Sympatec Helos laser diffraction instrument. Hall flow tests were carried out to evaluate the investigated powder flowability. Detailed information about the apparent as well as tapped density measurements could be found elsewhere [20].

A Concept Laser M2 cusing L-PBF machine was used to initially fabricate 10 mm-side cubes of the investigated powders to optimize processing parameters. The processing involved the application of 200 W laser on powder layers having a thickness of 40 μm. Meander scanning strategy was utilized, and the main variables were the hatching distance and the scanning velocity, according to the values reported in Table 2.

2.2. Metallographic characterization

To determine the optimum processing parameters, relative density evaluation was performed on polished vertical sections

Table 1
Chemical composition (in weight %) of the steel powders.

Alloy	Chemical Composition (wt.%)						Production Process
	C	Cr	Mo	Si	Mn	O	
G-4130	0.30	1.00	0.20	0.30	0.60	0.05	Gas Atomization
W-4130	0.30	1.10	0.28	0.45	0.044	0.29	Water Atomization

Table 2
Process parameters selected for the L-PBF consolidation of the investigated powders.

L-PBF Process Parameters	
Laser Power, W	200
Layer Thickness, μm	40
Hatching distance, μm	60 ,70, 80, 90
Scanning Velocity, mm/s	500, 550, 600, 650

of the L-PBF processed cubes, estimating the fraction of defects - from at least 8 optical micrographs of each parameter combination - by an image analysis software. The microstructural features were highlighted after etching the specimens with Nital and/or Picral reagents and characterized by a field-emission Zeiss Sigma 500 VP scanning electron microscope (FE-SEM) and energy dispersive spectrometry (EDS). Electron backscattered diffraction (EBSD) analysis were carried out with an accelerating voltage of 20 KV and step size of 0.35 μm or 0.10 μm for higher magnification. Channel 5 suite of Oxford HKL Technology was used for the post-processing of data and further analysis. The local misorientation, also known as Kernal average misorientation (KAM) method, was calculated to describe the strain gradient within the investigated steels. The calculations were carried out for every indexed pixel, in which an average misorientation angle between a pixel and its surrounding neighbors (8 pixels) was calculated and assigning a mean value for that pixel. It is to remark that misorientation angles greater than 5° were always neglected as stated elsewhere [33].

A Rigaku SmartLab X-Ray diffractometer (XRD) was used to perform phase analysis. X-rays were generated by a Cu-Kα radiation at 40 kV and 40 mA. The peaks of interest were scanned at 1°/min, at a resolution of 0.02°. The quantitative phase analysis was carried out by Rietveld refinement method using SmartLab Studio II software.

2.3. Calorimetric analysis and thermodynamic modelling

A Setaram Labsys differential scanning calorimeter (DSC) was adopted to perform the calorimetry analysis on the as-built specimens. The tests were carried out with a rate of 10 °C/min in an Argon atmosphere to determine the main phase transformation temperatures of the steels.

Identification of the DSC peaks and definition of other minor phases was assisted by thermodynamic equilibrium calculations based on the CALPHAD method. ThermoCalc AB software was used relying on TCFE9 and MOBFE4 Steel/Fe-alloy databases to conduct the simulations.

2.4. Post-process thermal treatments

Given the rapid solidification and high cooling rates promoted by the L-PBF process, two thermal treatment routes were selected consisting in tempering the structure from either as-built or conventionally quenched condition. Before quenching in water, both steels were initially austenitized at 840 °C for 1 h. The tempering levels ranged between 250 and 550 °C with a holding time of 1 h for both alternatives.

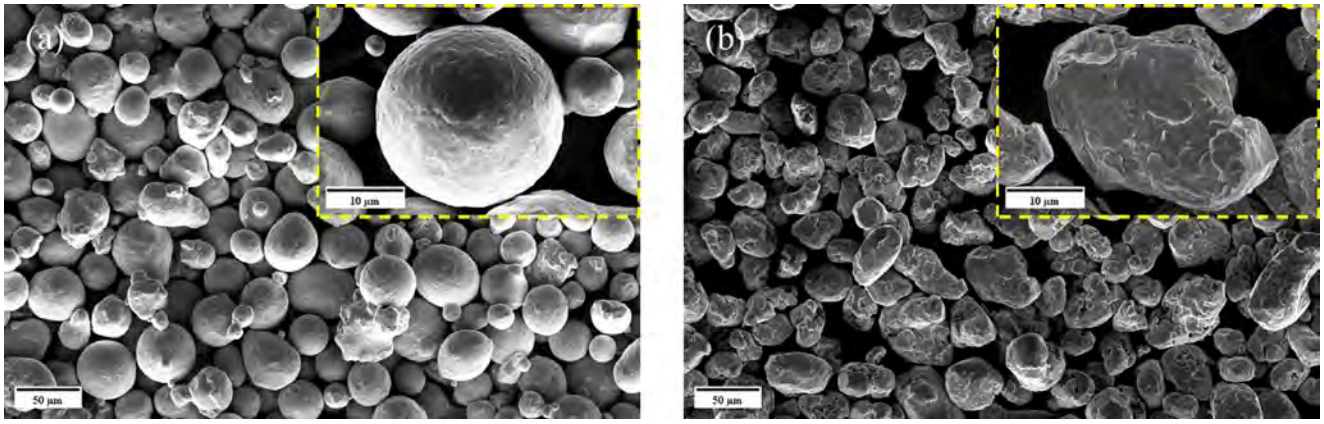

Fig. 1. FE-SEM images of (a) GA and (b) WA 4130 steel powder.

Table 3
Characteristics of the investigated powders.

Alloy	Particle Size Distribution (μm)			Flow (s/50 g)	ρ_{App} (g/cm^3)	ρ_{Tap} (g/cm^3)
	D_{10}	D_{50}	D_{90}			
G-4130	27	43	65	13.4	4.10	4.90
W-4130	20	38	61	21.9	3.41	4.22

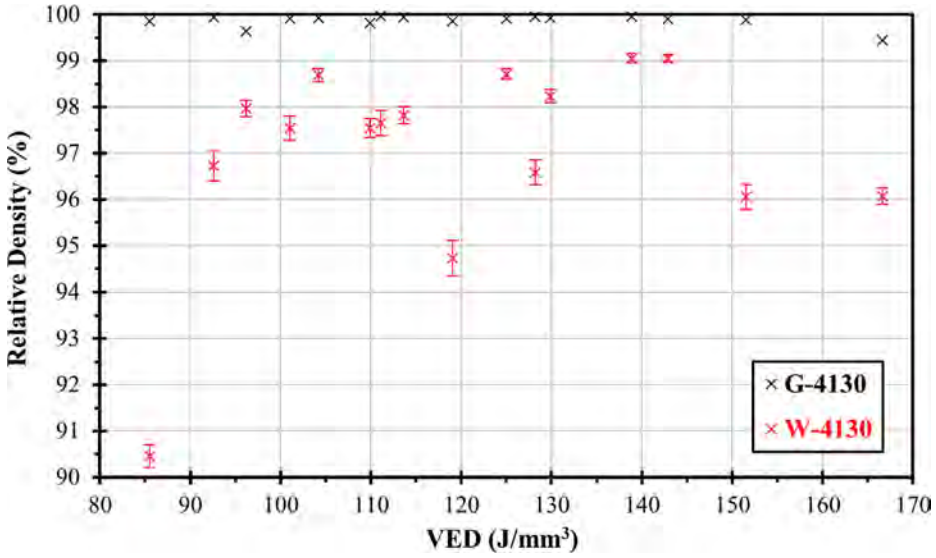

Fig. 2. Density of the L-PBF consolidated powders as a function of Volume Energy Density.

2.5. Mechanical testing

The mechanical properties of the investigated steels were studied by microhardness and tensile testing. Vickers' tests were performed using a Future Tech FM-700 machine by the application of 500 g_f load, for a dwell time of 15 s. Around 10 measurements per condition were performed to provide statistical data. Dog-bone tensile specimens having 10 mm diameter and a gauge length of 45 mm were machined from oversized samples fabricated by L-PBF using the optimum parameters for each alloy. The specimens

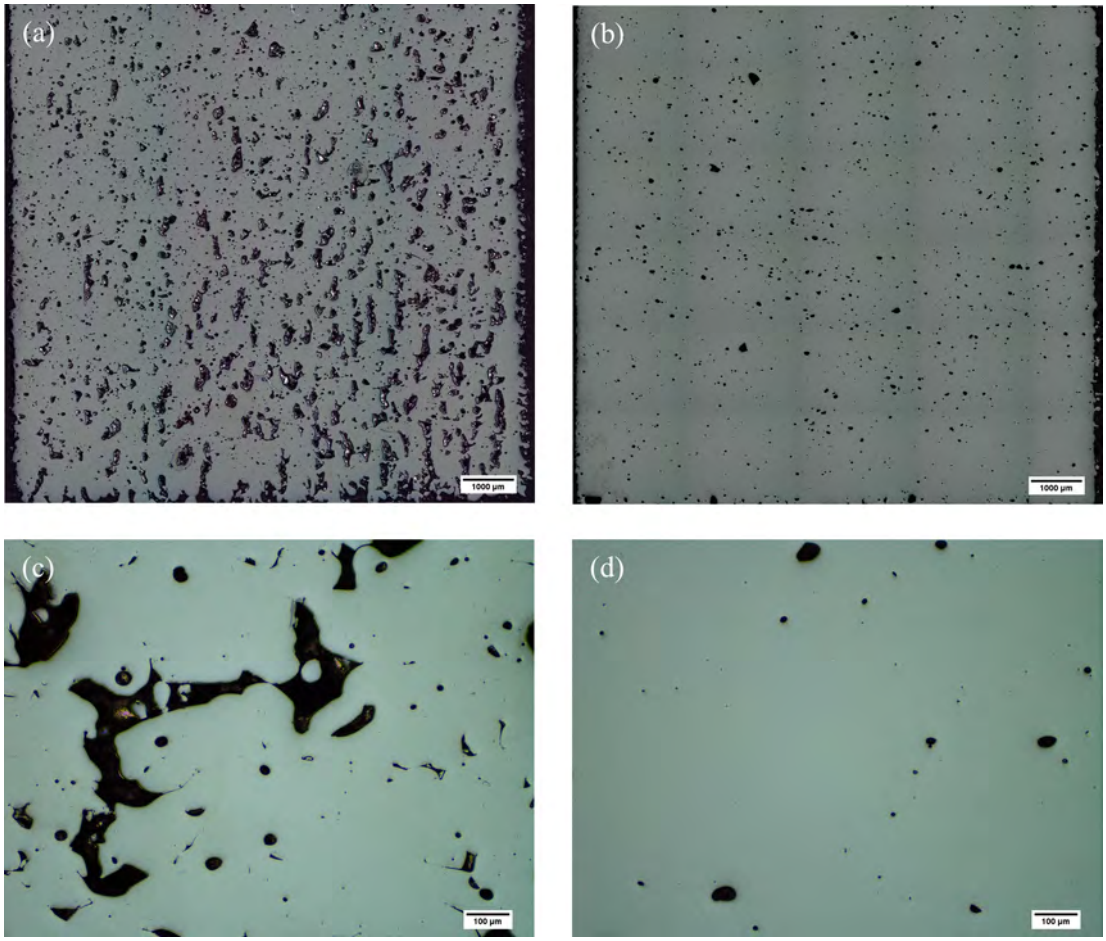

Fig. 3. Optical micrographs of W-4130 steel processed with (a, c) 85.5 J/mm^3 and (b, d) 129.9 J/mm^3 VEDs. Micrographs (c) and (d) are captured at higher magnification.

were tested by an MTS Alliance RT/100 universal testing machine according to ASTM E8M standard at room temperature and at initial strain rate of $0.6 \cdot 10^{-3}$ s^{-1}. At least two specimens for each condition were tested. Finally, a Zeiss EVO-50XVP SEM was adopted to scan the fracture surfaces of broken specimens to define the fracture mechanisms.

3. Results and discussion

3.1. Powder properties and relative density evaluation

The adoption of WA process to produce one of the steels investigated required a deliberate modification of the chemical compo-

Table 4
Main phase transformation temperatures of the 4130 steels.

	Method	A_{c3} / A_3 (°C)	T_c (°C)	B_s (°C)	M_s (°C)
G-4130	DSC	802	–	–	–
	TC	800	759	558	393
W-4130	DSC	815	769	–	–
	TC	811	765	568	434

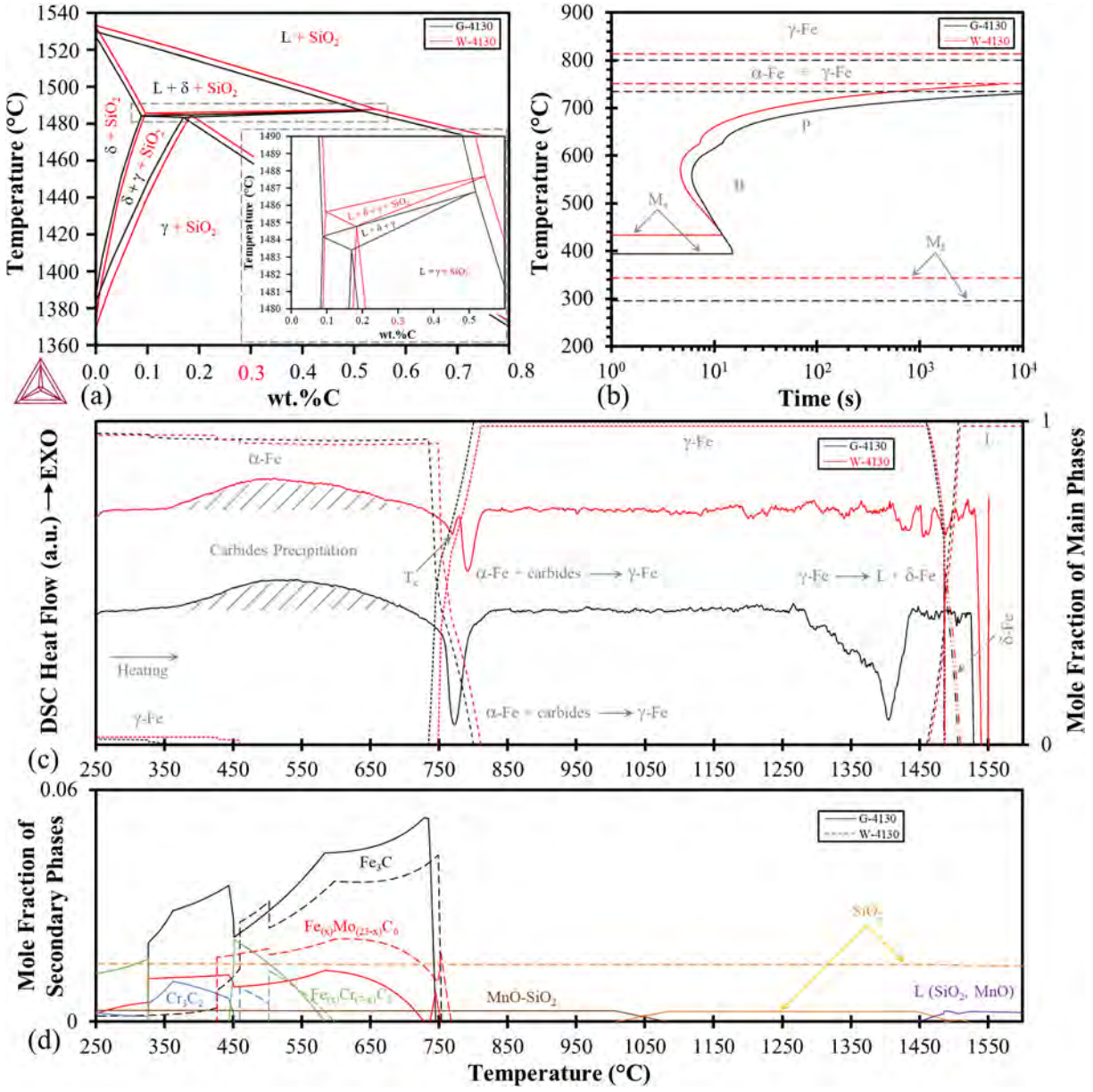

Fig. 4. (a) Phase diagram, (b) TTT curves, (c) DSC thermograms with calculated equilibrium phases against temperature, and (d) secondary phase evolution with temperature of the investigated steels.

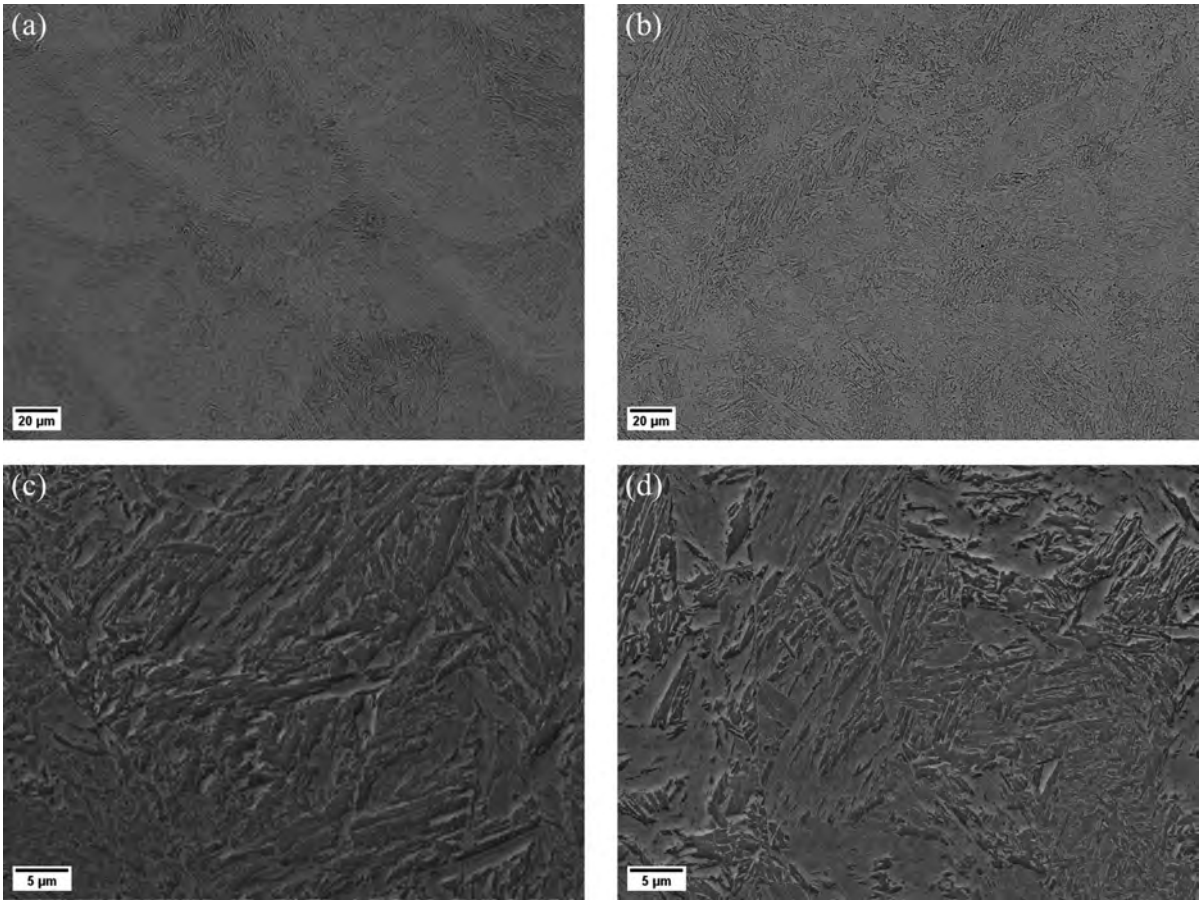

Fig. 5. As-built microstructure of (a and c) GA steel and (b and d) WA steel.

sition (Table 1), in order to reduce the amount of Mn, which would otherwise be easily oxidized [31]. The morphology of the investigated steel powders in both GA and WA conditions is displayed in Fig. 1. It is known that the atomization process utilizing water sprays results in a more irregular shape of the powder particle morphology due to the high solidification rate induced, estimated to be 10 to 100 times higher than that of GA [31]. Irregular-shaped powders can in turn impair powder flowability compared to the more spherical powders produced by GA. However, the WA particle shape could be improved by the adoption of a suitable post-atomization mechanical treatment with the main purpose of modifying the powder morphology by removing the large satellites and smoothing the particles surfaces, as shown in Fig. 1(b). After the post-treatment, the W-4130 powder characteristics were significantly enhanced reaching an apparent density just 17% below the GA powder, while the flowability hit a value of 21.9 s/50 g, as summarized in Table 3. It is noteworthy to mention that the powder flowability of similar low-alloy steels measured right after the WA process was in a range between 30.7 and 36.0 s/50 g [20].

A first assessment of L-PBF processability of the investigated steels powders is shown in Fig. 2 in terms of achieved densification as a function of the applied volume energy density (VED) calculated according to equation (1).

$$VED = \frac{P}{L_T * H_d * V} \quad (1)$$

Where P represents the laser power (W), L_T is the layer thickness (µm), H_d is the hatching distance (µm), and V is the laser scanning velocity (mm/s).

The results show that the GA steel leads to a high relative density over a wide range of VED values, while the WA powder is more prone to provide larger data scatter and to achieve slightly lower relative density values. Fig. 3 depicts polished vertical cross sections of the W-4130 specimens fabricated with different VEDs. It could be observed that a low heat input results in a poor consolidation of the WA powder and high fraction of lack of fusion defects. By increasing the VED value, improved densification was achieved, and only marginal gas induced porosity was detected. Based on the above-mentioned results, the G- and W-specimens fabricated with 111.1 and 129.9 J/mm^3 respectively, were considered for the further analyses.

3.2. Thermodynamic simulation

The main results of the thermodynamic simulations are summarized in Table 4 and in Fig. 4. Data are based on the hypotheses of phase stability under equilibrium (as calculated by ThermoCalc) for the phase diagrams are shown in Fig. 4(a), and on diffusion-assisted phase precipitation and isothermal transformations for the TTT diagrams are reported in Fig. 4(b). The experimental results of calorimetry tests (solid lines) are also displayed in Fig. 4(c) to ease the direct comparison with the equilibrium data (dashed lines). Finally, information about the carbides and other non-metallic compounds expected in the investigated steels is provided in Fig. 4(d).

From Fig. 4(a), it is observed that both steels experience substantially the same solidification mode, even though the lack of

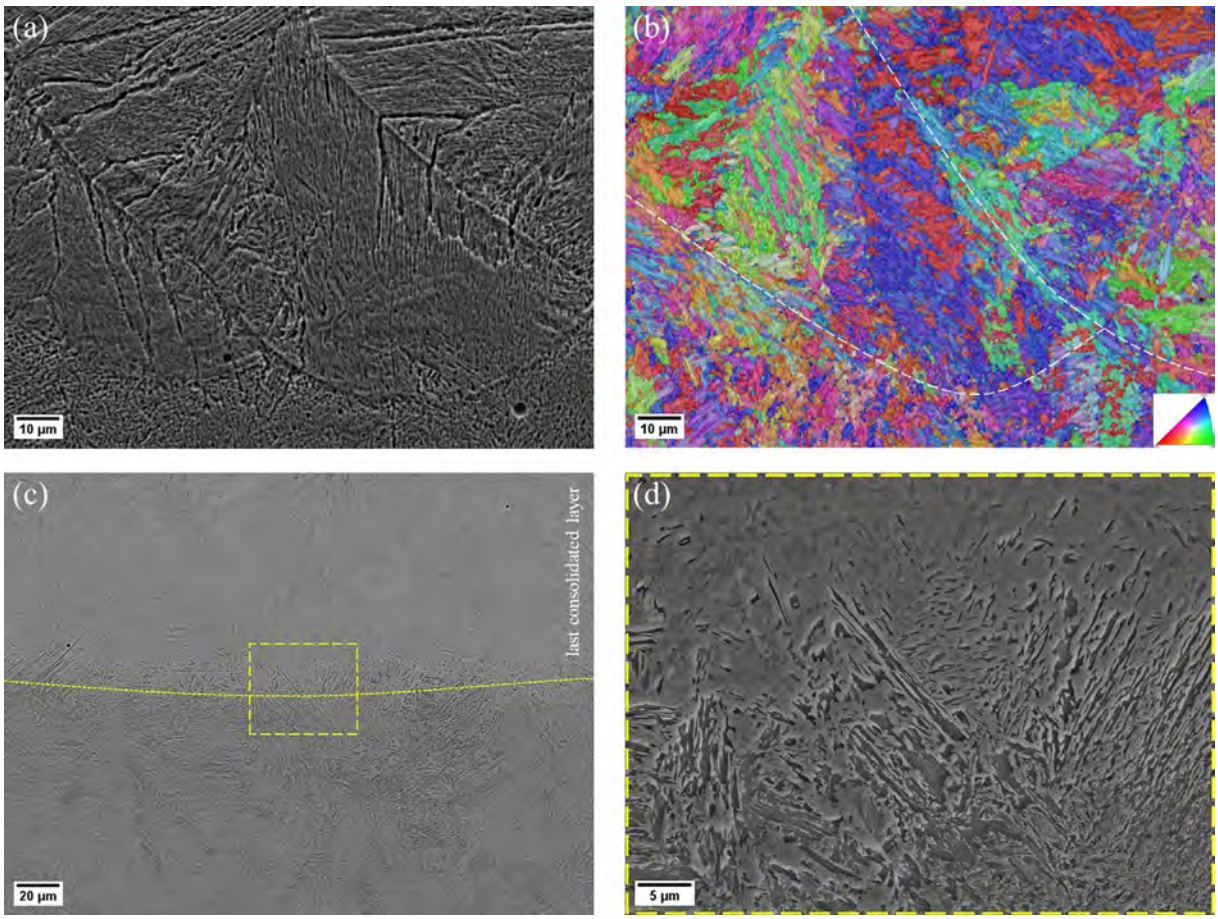

Fig. 6. (a) FE-SEM and (b) IPF on top layer of as-built W-4130 alloy. (c and d) FE-SEM of as-built G-4130 steel taken in region corresponding to boundary with the last deposited layer.

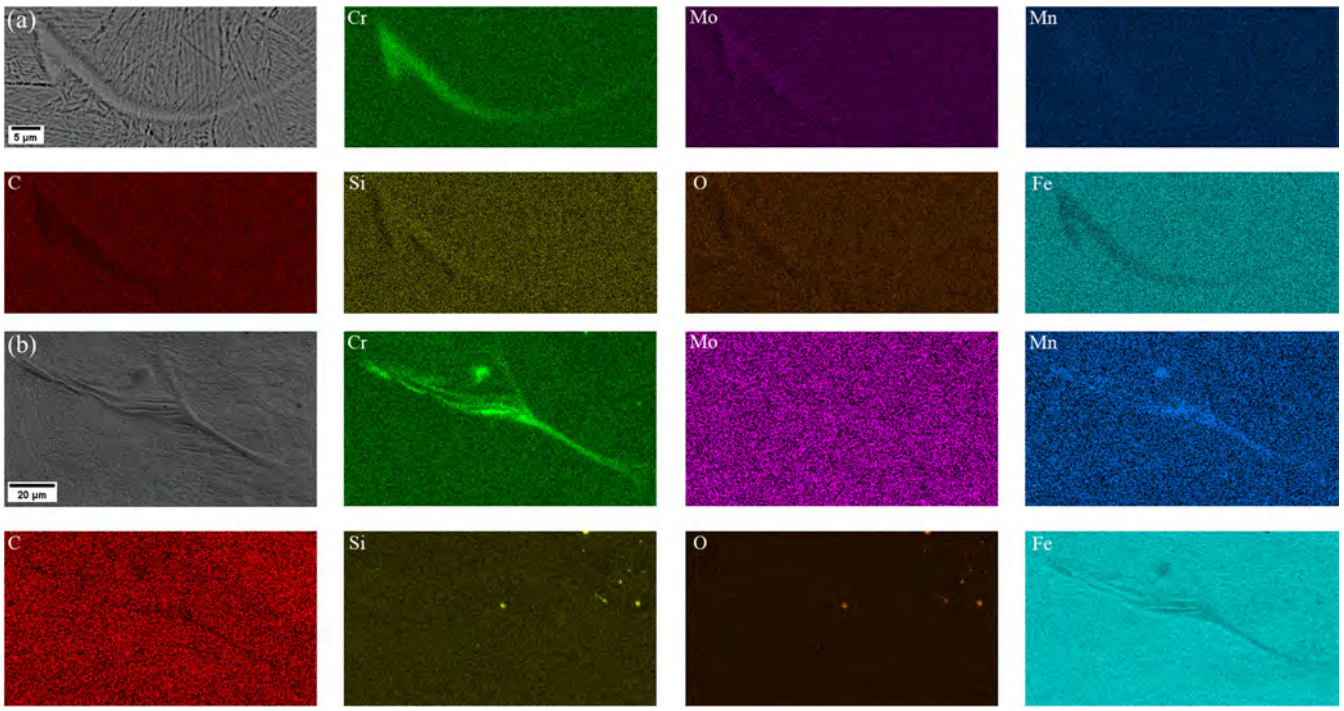

Fig. 7. EDS elemental maps for (a) G-4130 and (b) W-4130 steels in as-built condition.

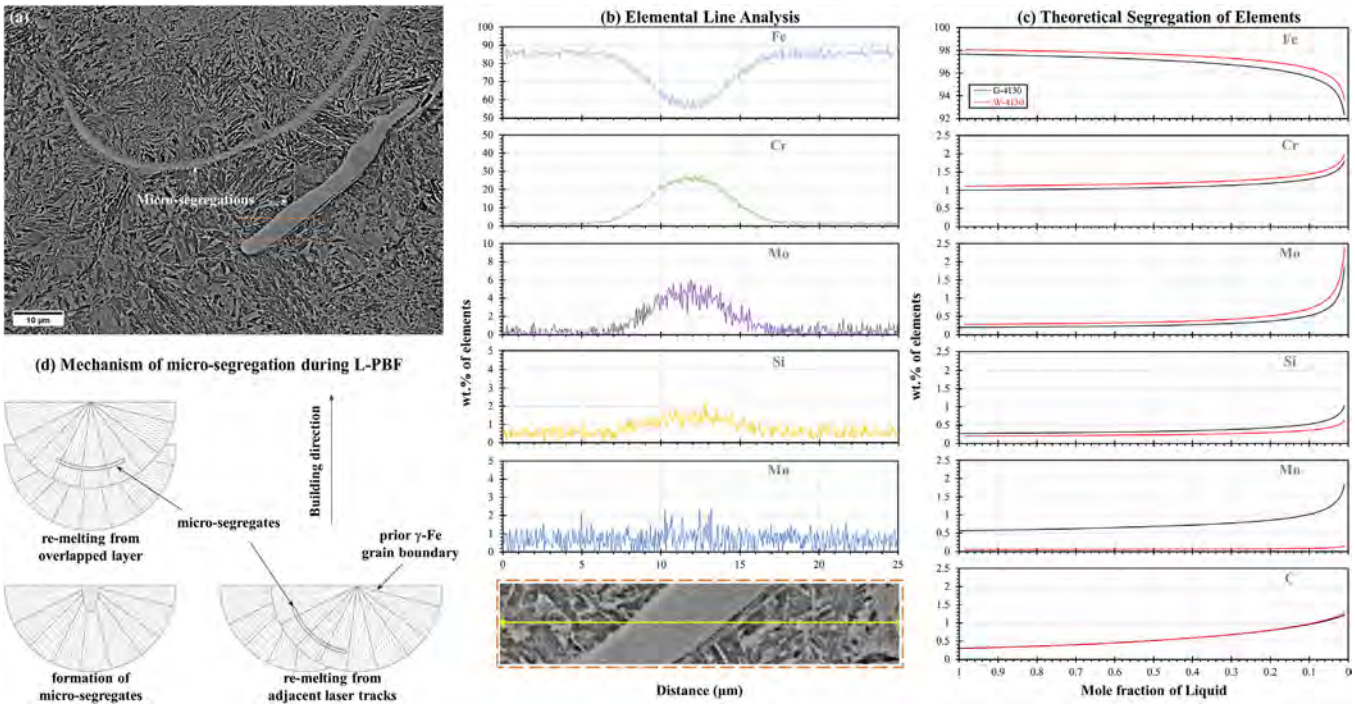

Fig. 8. A proposed micro-segregation mechanism in the investigated low alloy steels (a) reference FE-SEM micrograph of as-built G-4130, (b) EDS line analysis, (c) calculated amount of segregates during Scheil-Gulliver solidification hypotheses, (d) proposed model of microstructure evolution during track deposition by L-PBF.

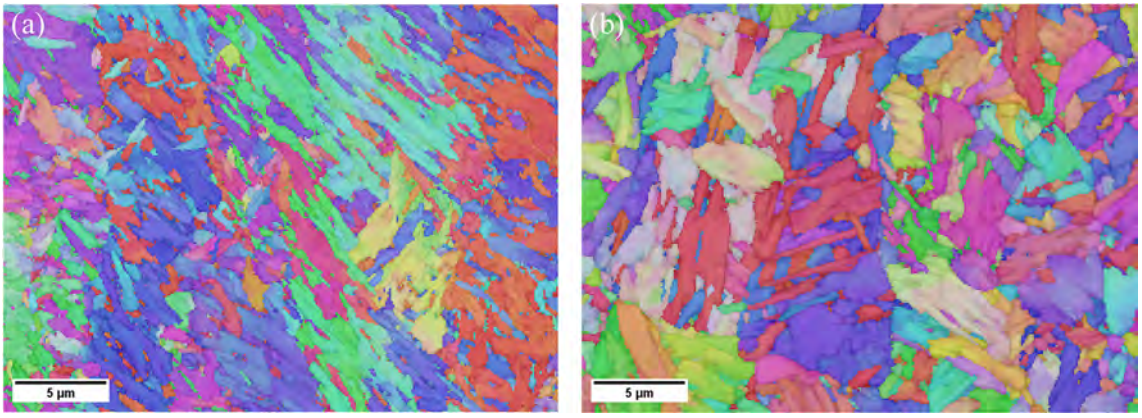

Fig. 9. IPF of W-4130 in (a) as-built and (b) as-quenched conditions.

manganese and the higher oxygen content of the W-steel tends to shift the main transformation lines to higher temperatures and contributes to the formation of SiO_2-based inclusion compared to the G-steel. Under equilibrium condition, both steels solidify by a hyper-peritectic sequence: L → L + δ-Fe → L + δ-Fe + γ-Fe → L + γ-Fe → γ-Fe.

The equilibrium data are in good agreement with the DSC results, even considering that the calorimetric tests have been conducted using finite heating rate of 10 °C/min. In the DSC thermograms of Fig. 4(c), heating of the investigated steels from the as-built condition results in precipitation of carbides over a wide range of temperatures. The thermodynamic simulations defined the possible precipitated carbides to be Cr_3C_2, $Fe_{(x)}Cr_{(7-x)}C_3$, $Fe_{(x)}Mo_{(23-x)}C_6$, and Fe_3C as displayed in Fig. 4(d). Further heating showed a ferromagnetic to paramagnetic transition of α-Fe, at the Curie temperature (T_c), that is clearly detected from W-4130 heat flow result at a temperature around 769 °C. Later, γ-Fe is formed by the transformation of α-Fe as well as the dissolution of precipitated carbides, and the A_{c3} transformation temperature was determined from the onset of the endothermic peaks to be around 802 °C and 815 °C for G-steel and W-steel, respectively. While under equilibrium, the A_3 temperature of G-4130 is 800 °C and 11 °C higher for the W-type steel. Moreover, the eutectoid reaction (from the equilibrium calculations) in the investigated steels occurs below 753 °C and 768 °C for G-4130 and W-4130, respectively, in which the pearlite is mainly formed by α-Fe and a mixture of type $Fe_{(x)}Mo_{(23-x)}C_6$ carbides with Fe_3C.

It can be noticed that the modified chemical composition of W-4130 results in a slight decrease of hardenability (earlier start of bainitic reaction in TTT curves of Fig. 4(b)) compared to the standard G-type steel. The displayed TTT curve of the W-steel is believed to be conservative, since the expected oxide-phase particles that could stimulate the nucleation of constituents other than martensite, were not considered during the calculations. Finally, it

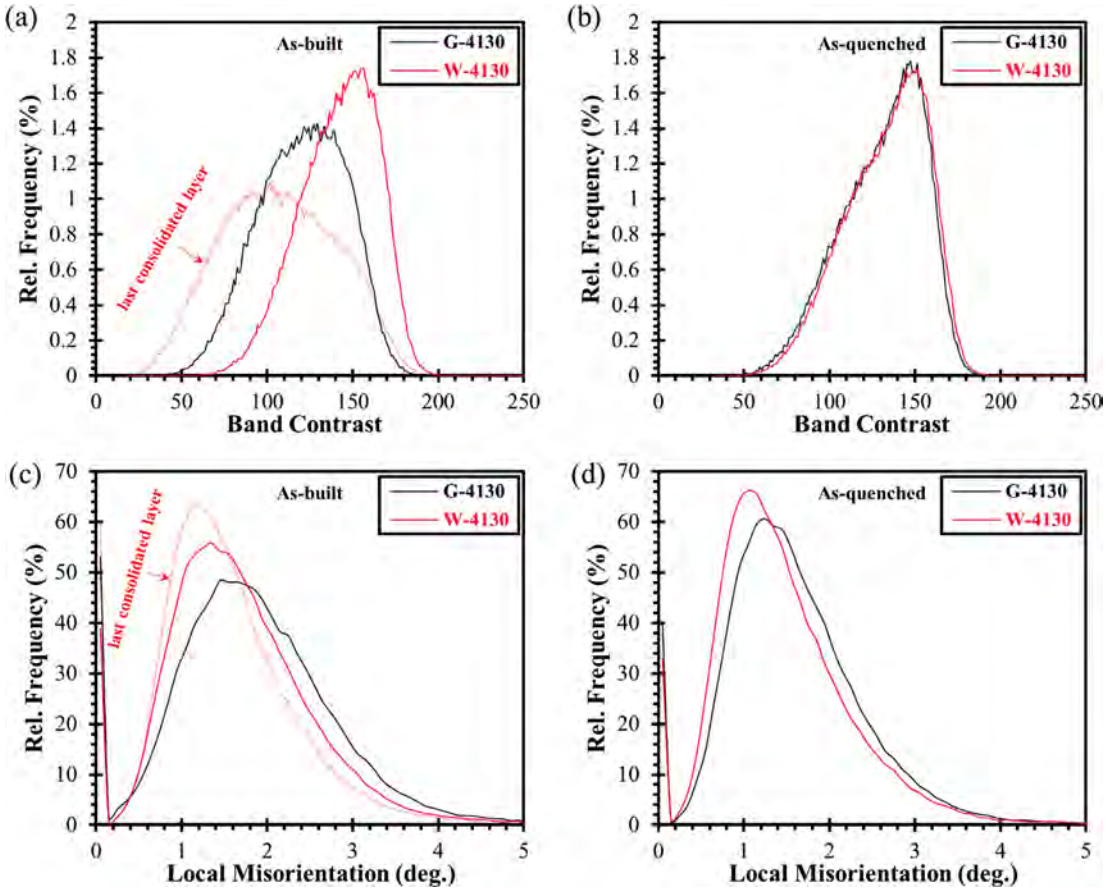

Fig. 10. Band contrast profiles for (a) as-built and (b) as-quenched steels, respectively. Local misorientation angles between (c) the as-built and (d) the as-quenched microstructures, respectively. EBSD results of the last consolidated powder layer correspond to analysis performed on a narrower area of 140 × 100 μm^2.

is to remark that the main phase transformation temperatures of W-4130 are shifted around 10 °C to 15 °C higher than those of the G-4130, while the difference become more significant in the martensitic reaction about 41 °C, as given in Table 4.

3.3. As-built microstructure

Fig. 5 and Fig. 6 display a collection of the 4130 steel microstructures obtained after the L-PBF process. All the micrographs refer to vertically cross-sectioned specimens (the vertical direction of the images is parallel to building direction, Z). The deposition of adjacent laser tracks as well as the melting of overlapped layers result in the formation of melt pools which are highlighted by the etching effect in the micrograph of Fig. 5(a). However, it can be observed that the melt pool boundaries are less visible in the as-built WA steel, as shown in Fig. 5(b), than in the GA steel. In addition, the higher magnification FE-SEM micrographs of Fig. 5(c) and 5(d) revealed that both 4130 steels exhibit similar microstructural features and were mainly composed of a partially tempered martensite.

For a better understanding of the microstructure generated directly after solidification from L-PBF processing, metallographic analysis was carried out focusing on the very last consolidated powder layer. The FE-SEM micrographs of Fig. 6(a) reveals the columnar shape of the prior austenitic grains (after etching with Picral reagent) growing in an epitaxial mode and roughly following the direction of thermal gradient, while the inverse pole figure (IPF) referred to the same location provided in Fig. 6(b) better shows the crystallographic orientation of martensitic laths across the melt pool boundaries. Fig. 6(c) and 6(d) specifically refer to the same situation found on top of the sample after etching with Nital reagent. It can be supposed that almost fresh martensitic structure is found in the top layer, as confirmed by the different microstructure appearance shown on top of the image, while a microstructure composed of tempered martensite and bainite is detected in the underlaying layers.

A careful analysis of the microstructure after L-PBF additionally reveals that micro-segregation of elements are present in both steels, as reported in Fig. 7. The EDS elemental analysis confirmed that Cr, Mn, and Mo (although to a lower extent) are the main elements involved in the segregation. It was found that such segregation contributed to a local increase in hardness, reaching peaks of 544 ± 11 HV for both alloys, as opposed to the average value of 505 ± 18 HV and 419 ± 19 HV found in non-segregated areas of G-steel and W-steel, respectively. Additionally, the EDS maps of Fig. 7(b) suggest that in the W-4130 steel, tiny inclusions rich in Si and O are found, consistently to the higher oxygen content and to the expected prediction of SiO_2 phase suggested by the thermodynamic simulations.

Fig. 8 depicts a proposed mechanism for the described micro-segregation of alloying elements during the laser processing of the investigated steels. To better understand the phenomenon, a set of EDS elemental line analyses were performed on the G-type steel in as-built condition, as shown in Fig. 8(b). In parallel, simulation of the segregation of elements during solidification was evaluated based on Scheil-Gulliver solidification model (Fig. 8(c)). It is assumed that the high cooling rates and the rapid solidification experienced by the steels limit the redistribution of solute atoms

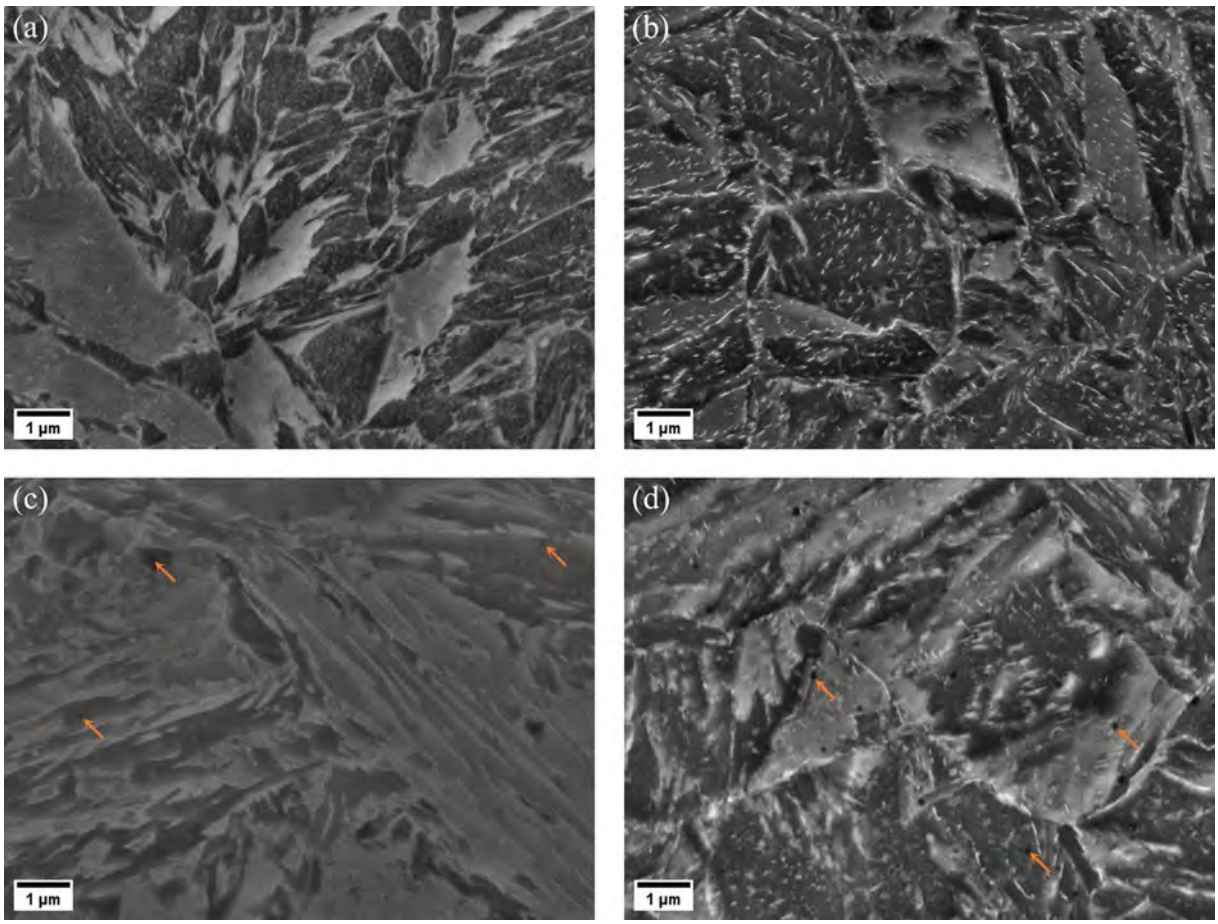

Fig. 11. High magnification FE-SEM micrographs of G-steel in (a) as-built and (b) quenched and tempered at 450 °C, W-steel in (c) as-built and (d) quenched and tempered at 450 °C.

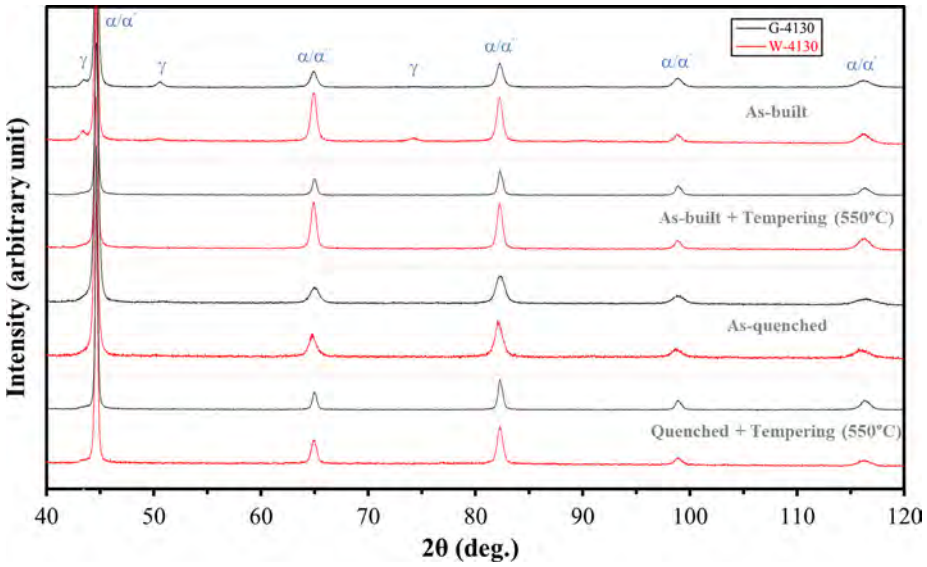

Fig. 12. XRD patterns of the investigated steels in different thermal treatment conditions.

in the solid, that tend to be rejected in the liquid phase, which in turn becomes richer in Cr, Mo, Si, and Mn atoms, resulting in segregation at regions corresponding to last stages of solidification. The following adjacent or overlapping laser tracks promote at least partial remelting of these solute-rich zones and, on some occasions, make evident the traces of a residual volume of segregation close to the newly formed melt pool boundaries (Fig. 8(d)). Finally, it is noteworthy that the solute concentration in the segregated

area is sharp, and that residual traces are occasionally observed even after the post-process thermal treatments, as described in the following text.

3.4. Post-process thermal treatments

The 4130 low-alloy steel grade has the ability to be hardened through the quenching and tempering (Q&T) treatment. The austenitizing stage was performed above the A_{C3} of both steels, at 840 °C, followed by quenching in water to obtain a martensitic structure. Tempering was then applied at different temperatures. An alternative and cheaper post-process thermal treatment was also proposed, consisting in the direct tempering starting from the as-built microstructure, considering that both 4130 steels already exhibit a martensitic matrix right after the L-PBF processing.

A qualitative comparison between the microstructure of the W-4130 steel in as-built and in as-quenched states is provided in Fig. 9. It could be observed that slightly finer microstructural constituents are presented in as-built condition compared to the as-quenched state, presumably due to higher cooling of the L-PBF process.

Further EBSD analysis were carried out to identify more precisely the microstructure of the investigated steels using the band contrast (BC) approach which has been widely exploited for distinguishing phases that are featuring similar crystal structures [34,35]. The grey-scale BC image is based on the electron backscattered patterns or the Kikuchi bands in which the phases with high imperfections, such as martensite, are more difficult to be indexed and result in low quality patterns as well as low values on a grey scale. The results of the BC approach for the investigated steels are given as raw data (i.e. without the influence of post-processing after data acquisition) in Fig. 10, and correspond to the analysis performed on a wide area (190 × 140 μm^2) to provide better statistical data for the 4130 steels in as-built and as-quenched conditions. In Fig. 10(a), the low BC values of the last consolidated powder layer suggest the presence of almost fresh martensite. Moreover, it could be observed that W-4130 after the L-PBF process provides an overall higher quality patterns than the G-4130, which suggests a slightly lower amount of martensite. This suggestion is consistent with the calculated TTT diagram shown in Fig. 4(b), which predicted a relatively lower hardenability in the W-4130 steel. After quenching, both steels showed almost identical BC profiles, as reported in Fig. 10(b). Quantitative analysis of the local misorientation in the two steels has been performed to highlight the local strain in as-built and as-quenched microstructures, Fig. 10(c) and 10(d) respectively. Higher residual stresses, indicated by local straining and higher misorientation values, were calculated for the as-built structure over those in as-quenched state. That is due to the rapid solidification as well as the high cooling rates experienced by the steels during the L-PBF process. Moreover, it is to remark that slightly lower residual stresses were found in the last consolidated layer, Fig. 10(c). The findings of Fig. 10(c) and 10(d) indicated lower local misorientation values for the W-4130 in any condition, which again confirmed the presence of a lower fraction of martensite compared to the G-steel. The results are in accordance with data published by Zhou et. al. [33] who measured higher local misorientation angles for martensite, compared to a mixed microstructure composed of martensite and bainite.

High magnification FE-SEM micrographs of the investigated steels are given in Fig. 11. It is confirmed that carbides are already present in the as-built microstructure since the heat generated during the laser processing of successive powder layers contributes

Table 5
FWHM (100) α/α' of the investigated 4130 steels in different conditions.

	As-built	As-built and Tempered	As-quenched	Quenched and Tempered
G-4130	0.313 ± 0.001	0.205 ± 0.001	0.429 ± 0.002	0.203 ± 0.001
W-4130	0.267 ± 0.002	0.248 ± 0.002	0.339 ± 0.003	0.252 ± 0.002

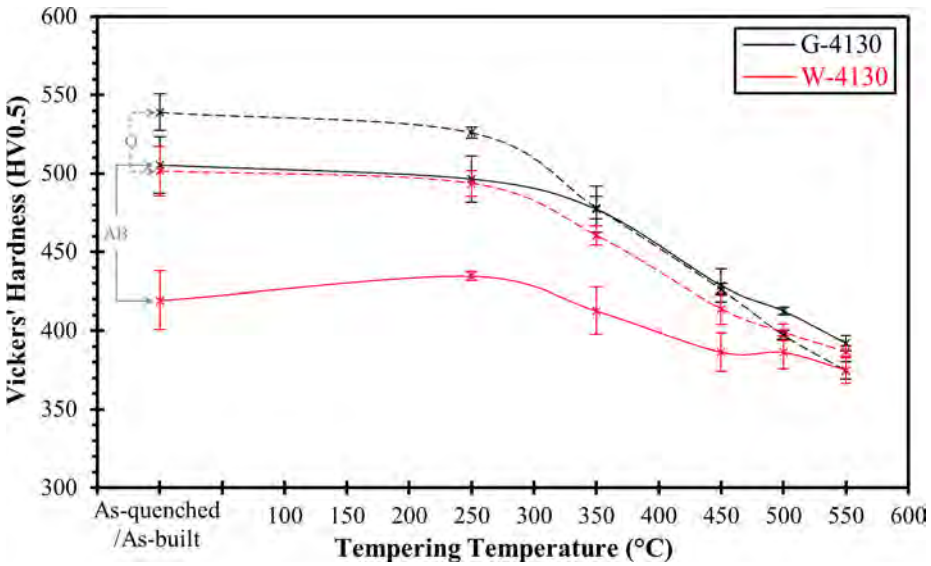

Fig. 13. Vickers' hardness as a function of the tempering temperature for the 4130 steels.

Table 6
Tensile data of the investigated 4130 steels.

	Specimen Orientation	Treatment Condition	YS (MPa)	UTS (MPa)	Fracture Elong. (%)
G-4130	XY	AB	1249 ± 15	1419 ± 30	3.4 ± 0.6
		AB + T	1076 ± 45	1127 ± 58	2.1 ± 0.0
		Q + T	1118 ± 4	1170 ± 10	6.4 ± 1.0
	Z	AB	1166 ± 5	1277 ± 7	6.3 ± 0.9
		AB + T	1057 ± 11	1124 ± 11	7.9 ± 1.3
		Q + T	1125 ± 1	1177 ± 1	7.9 ± 0.5
W-4130	XY	AB	1072 ± 2	1168 ± 17	2.5 ± 0.1
		AB + T	1019 ± 6	1066 ± 13	2.6 ± 0.3
		Q + T	1099 ± 17	1120 ± 15	1.9 ± 0.1
	Z	AB	981 ± 4	1059 ± 13	3.2 ± 1.5
		AB + T	952 ± 8	1012 ± 19	4.2 ± 2.2
		Q + T	1110 ± 10	1123 ± 15	1.4 ± 0.4

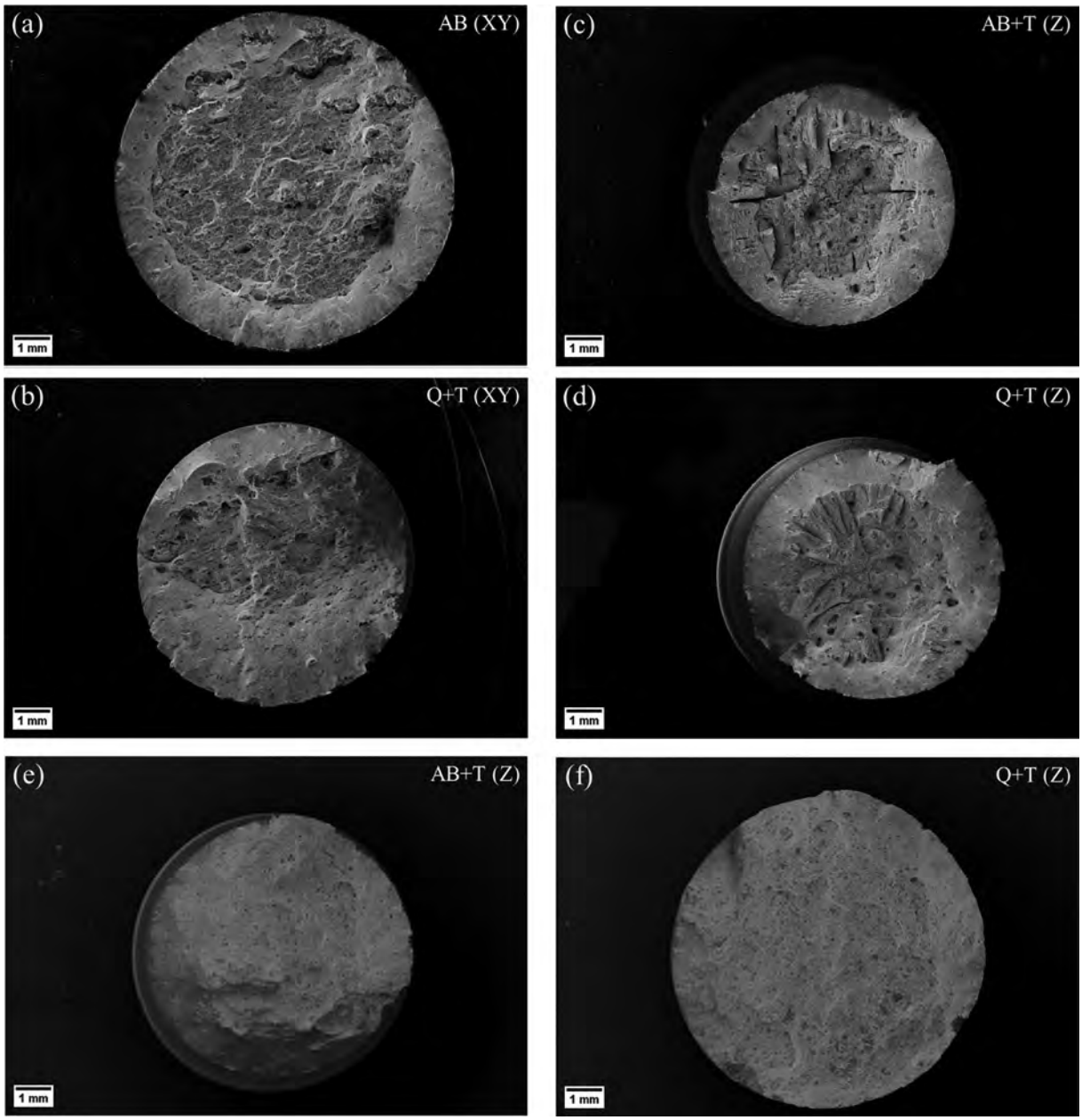

Fig. 14. Low magnification fracture surfaces of (a-d) G-4130 and (e-f) W-4130 steels in different treatment conditions.

to an in-situ tempering effect. The application of a conventional quench and tempering treatment resulted in a higher fraction of carbides having a needle-like shape that were found within the martensitic laths and decorating the lath boundaries. The thermodynamic simulations expected that carbides of type Fe_3C, $Fe_{(x)}Mo_{(23-x)}C_6$, $Fe_{(x)}Cr_{(7-x)}C_3$, as well as Cr_3C_2 are stable at the temperature range between 350 °C and 550 °C. Additionally, the tiny black dots (marked with arrows) in the micrographs of W-steel refer to the oxide-based inclusions that were discussed previously. The spherical-shape of those dispersed non-metallic inclusions also support the hypotheses of SiO_2 formation above the melting temperature as defined from the thermodynamic calculations.

XRD patterns of the 4130 steels in different thermal treatment conditions are collected in Fig. 12. The analysis shows a significant amount of retained austenite, estimated according to Rietveld method to be about 8% and 10% for GA and WA steels, respectively, in the as-built condition. The peaks related to retained austenite were not detected after water quenching. As expected, broader α/α' phase peaks are found in the as-quenched state and become sharper after the tempering treatment, as quantitatively confirmed by the full width at half maximum (FWHM) values collected in Table 5. Consequently, it is believed that the as-built microstructure is somehow in an intermediate condition between the as-quenched and the quenched and tempered states.

3.5. Mechanical properties

The effect of tempering temperature on the microhardness evolution in the investigated steels is represented in Fig. 13. As expected, the general trend shows the softening of the alloys upon increasing the tempering temperature, with the G-steel showing systematically higher hardness than the WA counterpart. In case of as-quenched condition, the equilibrium thermodynamic simulations performed at 840 °C defined high fraction of SiO_2 around 1.6% in W-4130 and a negligible fraction of MnO-SiO_2 in G-4130, which turns into a relatively lower fraction of martensite as well as lower as-quenched hardness in the former steel. Moreover, higher microhardness values are measured for the tempered steels starting from a quenched structure compared to the corresponding as-built and tempered samples. It could be observed that the as-built W-steel is less sensitive to the tempering effects in terms of microhardness variation compared to the G-4130. Moreover, a significant hardness difference is detected between the as-quenched and the as-built W-steel, in comparison with the G-4130. It can be stated that the hardness of G-steel in as-built condition is comparable to hardness after quenching and tempering at temperatures below 350 °C, while for the W-steel the as-built state is almost equivalent to quenching and tempering at about 450 °C.

Tensile tests have been carried out on the L-PBF 4130 steels in as-built condition and after quenching and tempering or direct tempering from as-built state, selecting a tempering treatment carried out at 550 °C for 1 h. The data obtained are summarized in Table 6. The effects of specimen orientation, namely horizontal (XY) and vertical (Z) have been also investigated.

The AB as well as the AB + T horizontal specimens always provided the highest yield and tensile strength compared to the vertical specimens. On the contrary, improved fracture elongation was observed for the vertical specimens. By performing the conventional quenching and tempering treatment, more isotropic properties could be achieved, resulting in comparable properties in the two directions.

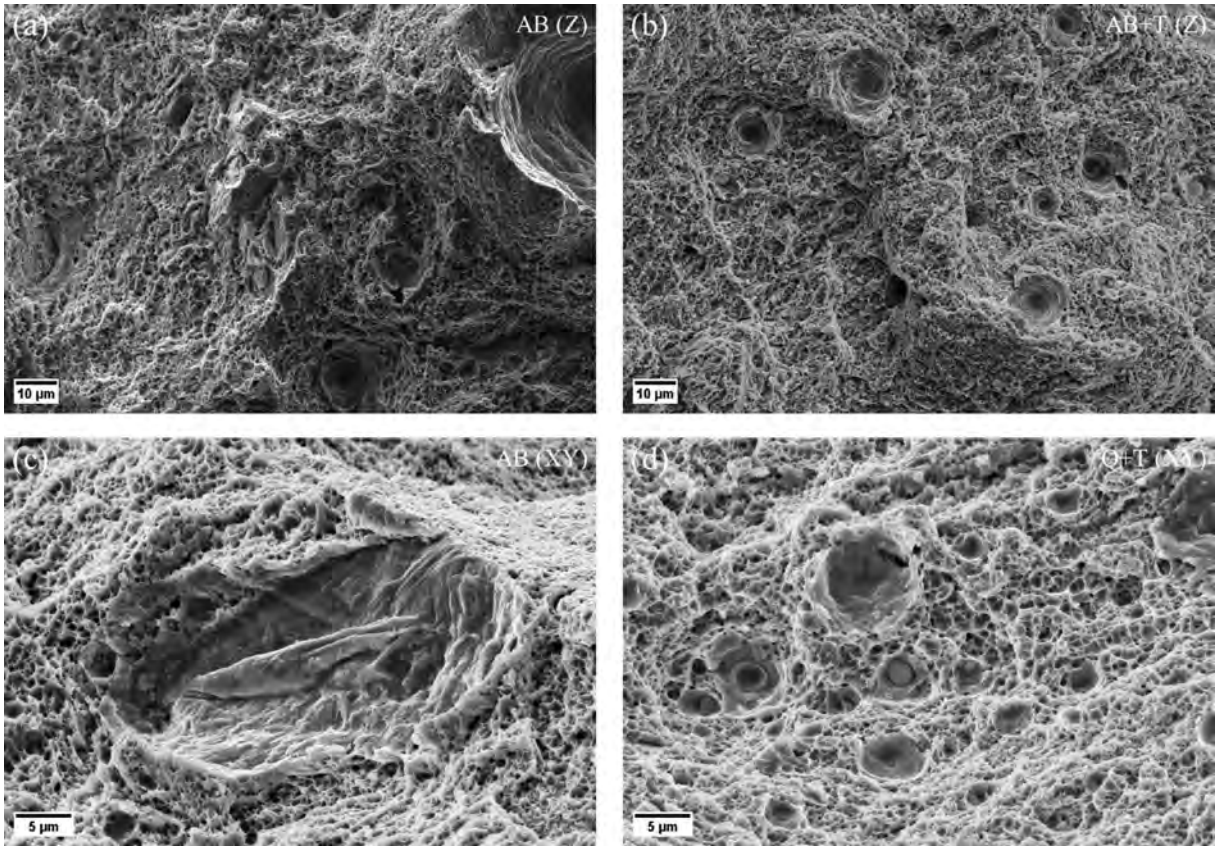

Fig. 15. High magnification fractographs of (a) G-steel and (b-d) W-steel.

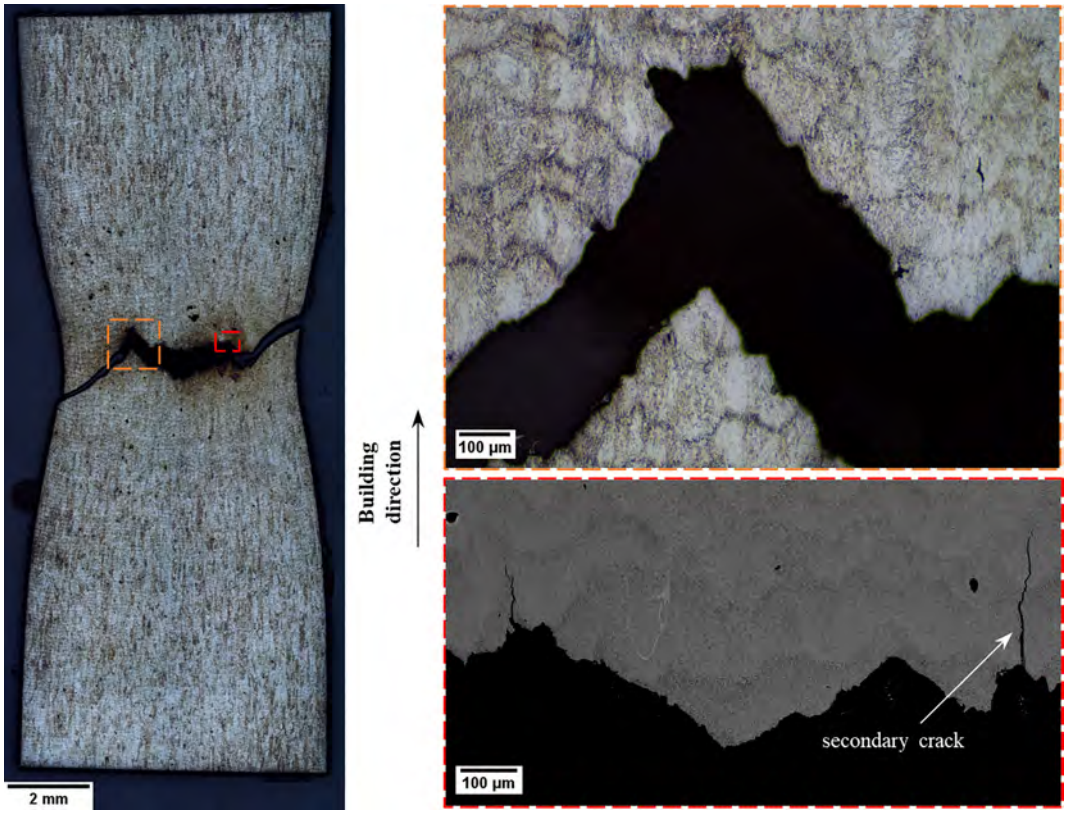

Fig. 16. Optical and FE-SEM on a cross-section of broken G-4130 vertical tensile specimen in as-built condition.

Regarding the combined effects of powder atomization process and chemical composition on mechanical properties, it can be observed that the G-steel delivered higher tensile properties over the W-steel in AB and AB + T conditions, due to the relatively lower amount of martensite in the latter steel, while the gap was again reduced after quenching and tempering.

3.6. Fractography

Fig. 14 displays representative fractographs of the investigated steels tested according to different orientations and thermal treatments. The XY specimens experienced a relatively lower plastic deformation and reduction of section induced by necking in agreement with the lower fracture elongations recorded. Moreover, high density of secondary cracks was observed on the fractographs of vertical specimens, especially for the G-4130 steel, Fig. 14(c) and 14(d).

Higher magnification images confirmed that both steels failed in a ductile manner by the growth of fine dimples, as displayed in Fig. 15(a) and 15(b). Occasionally, the solute-enriched regions already highlighted in Fig. 7 were found on bottom of relatively large and smooth craters, as shown in Fig. 15(c). As previously mentioned, the higher amount of oxygen in the WA steel contributed to the formation of SiO_2-based inclusions that were often found inside micro-voids (see Fig. 15(d)). Those non-metallic inclusions are believed to be effective sites for the early nucleation of sub-micrometer dimples and activated the ductile fracture mechanism during tensile testing.

Fig. 16 depicts a longitudinal cross section of a broken vertical specimen of the G-steel in as-built condition. The enlarged images in Fig. 16 reveal that both the main crack leading to specimen failure and secondary cracks generally propagated crossing the melt pools.

4. Conclusions

An investigation was performed on gas atomized and water atomized 4130-grade low-alloy steels processed by the Laser-Powder Bed Fusion. The main findings of the current study can be summarized as follows:

- Both steels showed a good L-PBF processability with high densification level and crack-free specimens. The water atomized steel could reach a relative density as high as 99%, whereas the gas atomized steel hit a level of 99.9%.
- The investigated steels showed substantially similar metallurgical features, resulting in the formation of partially tempered martensite with significant amount of retained austenite in the as-built condition. One of the main differences between the two steels is the relatively lower hardenability of the water atomized variant which was expected based on the variation of chemical composition. Moreover, the higher oxygen content of the water atomized steel contributed to the formation of SiO_2 inclusions which were observed in the microstructure and on the fracture surfaces. It was found that those non-metallic inclusions are of sub-micrometric size and contributed to the ductile fracture mechanism by nucleating sub-micrometer dimples.
- Some alloying elements such as Cr, Mn and Mo tended to segregate during fast solidification induced by the laser processing. As a result of this segregation and of the repeated remelting upon deposition of adjacent laser tracks and overlapping layers, solute-rich regions were found in the microstructure. A model to justify their position and shape was proposed.
- Anisotropic tensile properties were measured for both steels in the as-built condition and after performing a direct tempering treatment at 550 °C. Under these conditions, the horizontal

specimens showed higher strength but lower ductility than samples oriented along the vertical direction. After the quenching and tempering treatment, the anisotropy was almost suppressed since both steels showed substantially a similar tensile strength, apart from the reduced ductility of WA steel.

The general results also confirm the opportunity of using water atomized steel powders for the manufacturing of parts by L-PBF, especially when the production of large batches of powder make the water atomization route cheaper than the conventional gas atomization.

Declaration of Competing Interest

The authors declare that they have no known competing financial interests or personal relationships that could have appeared to influence the work reported in this paper.

Acknowledgements

The current investigation was performed in the frame of the joint research project SPAcEMAN - Sustainable Powders for AdditivE MANufacturing, funded by EIT-Raw Materials in 2018-2021. The authors would like to acknowledge the Italian Ministry of Education, University and Research for the support provided through the project "Department of Excellence LIS4.0 - Lightweight and Smart Structures for Industry 4.0".

Marawan Abdelwahed is funded by a full Ph.D. scholarship from the Ministry of Higher Education of the Arab Republic of Egypt.

Ludovica Rovatti and Michael Ishola are also acknowledged for their technical support at Politecnico di Milano.

Data availability

The raw/processed data required to reproduce these findings cannot be shared at this time as the data also forms part of an ongoing study.

References

[1] T. DebRoy, H.L. Wei, J.S. Zuback, T. Mukherjee, J.W. Elmer, J.O. Milewski, A.M. Beese, A. Wilson-Heid, A. De, W. Zhang, Additive manufacturing of metallic components – Process, structure and properties, Prog. Mater. Sci. 92 (2018) 112–224, https://doi.org/10.1016/j.pmatsci.2017.10.001.

[2] W.J. Sames, F.A. List, S. Pannala, R.R. Dehoff, S.S. Babu, The metallurgy and processing science of metal additive manufacturing, Int. Mater. Rev. 61 (5) (2016) 315–360, https://doi.org/10.1080/09506608.2015.1116649.

[3] P. Bajaj, A. Hariharan, A. Kini, P. Kürnsteiner, D. Raabe, E.A. Jägle, Steels in additive manufacturing: A review of their microstructure and properties, Mater. Sci. Eng. A. 772 (2020) 138633, https://doi.org/10.1016/j.msea.2019.138633.

[4] L. Cui, S. Jiang, J. Xu, R.L. Peng, R.T. Mousavian, J. Moverare, Revealing relationships between microstructure and hardening nature of additively manufactured 316L stainless steel, Mater. Des. 198 (2021) 109385, https://doi.org/10.1016/j.matdes.2020.109385.

[5] M.J. Heiden, L.A. Deibler, J.M. Rodelas, J.R. Koepke, D.J. Tung, D.J. Saiz, B.H. Jared, Evolution of 316L stainless steel feedstock due to laser powder bed fusion process, Addit. Manuf. 25 (2019) 84–103, https://doi.org/10.1016/j.addma.2018.10.019.

[6] R. Casati, J. Lemke, M. Vedani, Microstructure and Fracture Behavior of 316L Austenitic Stainless Steel Produced by Selective Laser Melting, J. Mater. Sci. Technol. 32 (8) (2016) 738–744, https://doi.org/10.1016/j.jmst.2016.06.016.

[7] B. Zhang, L. Dembinski, C. Coddet, The study of the laser parameters and environment variables effect on mechanical properties of high compact parts elaborated by selective laser melting 316L powder, Mater. Sci. Eng. A. 584 (2013) 21–31, https://doi.org/10.1016/j.msea.2013.06.055.

[8] A. Ben-Artzy, A. Reichardt, J.-P. Borgonia, R.P. Dillon, B. McEnerney, A.A. Shapiro, P. Hosemann, Compositionally graded SS316 to C300 Maraging steel using additive manufacturing, Mater. Des. 201 (2021) 109500, https://doi.org/10.1016/j.matdes.2021.109500.

[9] H. Irrinki, J.S.D. Jangam, S. Pasebani, S. Badwe, J. Stitzel, K. Kate, O. Gulsoy, S.V. Atre, Effects of particle characteristics on the microstructure and mechanical properties of 17–4 PH stainless steel fabricated by laser-powder bed fusion, Powder Technol. 331 (2018) 192–203, https://doi.org/10.1016/j.powtec.2018.03.025.

[10] R. Casati, J. Lemke, A. Tuissi, M. Vedani, Aging Behaviour and Mechanical Performance of 18-Ni 300 Steel Processed by Selective Laser Melting, Metals (Basel). 6 (2016) 218, https://doi.org/10.3390/met6090218.

[11] T. LeBrun, T. Nakamoto, K. Horikawa, H. Kobayashi, Effect of retained austenite on subsequent thermal processing and resultant mechanical properties of selective laser melted 17–4 PH stainless steel, Mater. Des. 81 (2015) 44–53, https://doi.org/10.1016/j.matdes.2015.05.026.

[12] M. Abdelwahed, S. Bengsston, R. Casati, A. Larsson, M. Vedani, L-PBF Processing of Steel Powders Produced by Gas and Water AtomizationL-PBF Verarbeitung von Stahlpulvern hergestellt durch Gas- und Wasseratomisierung, BHM Berg- Huettenmaenn. Monatsh. 166 (1) (2021) 40–45, https://doi.org/10.1007/s00501-020-01071-1.

[13] S. Bengtsson, R. Casati, A. Larsson, M. Riccio, M. Abdelwahed, M. Vedani, Design of structural low-alloy steels for laser-powder bed fusion, in, Euro PM 2019 Congr. Exhib. (2019) 1–8. http://hdl.handle.net/11311/1121733.

[14] W. Wang, S. Kelly, A Metallurgical Evaluation of the Powder-Bed Laser Additive Manufactured 4140 Steel Material, JOM. 68 (3) (2016) 869–875, https://doi.org/10.1007/s11837-015-1804-y.

[15] J. Damon, R. Koch, D. Kaiser, G. Graf, S. Dietrich, V. Schulze, Process development and impact of intrinsic heat treatment on the mechanical performance of selective laser melted AISI 4140, Addit. Manuf. 28 (2019) 275–284, https://doi.org/10.1016/j.addma.2019.05.012.

[16] Y.R. Han, C.H. Zhang, X. Cui, S. Zhang, J.B. Zhang, Y. Liu, The formability and microstructure evolution of 24CrNiMo alloy steel fabricated by selective laser melting, Vacuum 175 (2020) 109297, https://doi.org/10.1016/j.vacuum.2020.109297.

[17] J.J.S. Dilip, G.D.J. Ram, T.L. Starr, B. Stucker, Selective laser melting of HY100 steel: Process parameters, microstructure and mechanical properties, Addit. Manuf. 13 (2017) 49–60, https://doi.org/10.1016/j.addma.2016.11.003.

[18] L. Zumofen, A. Kirchheim, H.-J. Dennig, Laser powder bed fusion of 30CrNiMo8 steel for quenching and tempering: examination of the processability and mechanical properties, Prog. Addit. Manuf. 5 (1) (2020) 75–81, https://doi.org/10.1007/s40964-020-00121-x.

[19] E. Jelis, M. Hespos, S.L. Groeschler, R. Carpenter, L-PBF of 4340 Low Alloy Steel: Influence of Feedstock Powder, Layer Thickness, and Machine Maintenance, J. Mater. Eng. Perform. 28 (2) (2019) 693–700, https://doi.org/10.1007/s11665-018-3739-2.

[20] M. Abdelwahed, R. Casati, S. Bengtsson, A. Larsson, M. Riccio, M. Vedani, Effects of powder atomisation on microstructural and mechanical behaviour of l-pbf processed steels, Metals (Basel). 10 (11) (2020) 1474, https://doi.org/10.3390/met10111474.

[21] C. Lindemann, U. Jahnke, M. Moi, R. Koch, Analyzing product lifecycle costs for a better understanding of cost drivers in additive manufacturing, in: 23rd Annu. Int. Solid Free. Fabr. Symp. - An Addit. Manuf. Conf. SFF 2012, 2012: pp. 177–188.

[22] D.F. Heaney, Powders for metal injection molding (MIM), Handb. Met. Inject. Molding (2012), https://doi.org/10.1533/9780857096234.1.50.

[23] B.o. Song, S. Dong, S. Deng, H. Liao, C. Coddet, Microstructure and tensile properties of iron parts fabricated by selective laser melting, Opt. Laser Technol. 56 (2014) 451–460, https://doi.org/10.1016/j.optlastec.2013.09.017.

[24] M. Letenneur, V. Brailovski, A. Kreitcberg, V. Paserin, I. Bailon-Poujol, Laser Powder Bed Fusion of Water-Atomized Iron-Based Powders: Process Optimization, J. Manuf. Mater. Process. 1 (2) (2017) 23, https://doi.org/10.3390/jmmp1020023.

[25] R. Li, Y. Shi, Z. Wang, L.i. Wang, J. Liu, W. Jiang, Densification behavior of gas and water atomized 316L stainless steel powder during selective laser melting, Appl. Surf. Sci. 256 (13) (2010) 4350–4356, https://doi.org/10.1016/j.apsusc.2010.02.030.

[26] R.P. Koseski, P. Suri, N.B. Earhardt, R.M. German, Y.-S. Kwon, Microstructural evolution of injection molded gas- and water-atomized 316L stainless steel powder during sintering, Mater. Sci. Eng. A. 390 (1-2) (2005) 171–177, https://doi.org/10.1016/j.msea.2004.08.002.

[27] S. Cacace, Q. Semeraro, Influence of the atomization medium on the properties of stainless steel SLM parts, Addit. Manuf. 36 (2020) 101509, https://doi.org/10.1016/j.addma.2020.101509.

[28] M. Ghayoor, S.B. Badwe, H. Irrinki, S.V. Atre, S. Pasebani, Water Atomized 17–4 PH Stainless Steel Powder as a Cheaper Alternative Powder Feedstock for Selective Laser Melting, Mater. Sci. Forum. 941 (2018) 698–703, https://doi.org/10.4028/www.scientific.net/MSF.941.698.

[29] H. Irrinki, M. Dexter, B. Barmore, R. Enneti, S. Pasebani, S. Badwe, J. Stitzel, R. Malhotra, S.V. Atre, Effects of Powder Attributes and Laser Powder Bed Fusion (L-PBF) Process Conditions on the Densification and Mechanical Properties of 17–4 PH Stainless Steel, JOM. 68 (3) (2016) 860–868, https://doi.org/10.1007/s11837-015-1770-4.

[30] H.Ö. Gülsoy, S. Özbek, T. Baykara, Microstructural and mechanical properties of injection moulded gas and water atomised 17–4 PH stainless steel powder, Powder Metall. 50 (2) (2007) 120–126, https://doi.org/10.1179/174329007X153288.

[31] S. Hoeges, A. Zwiren, C. Schade, Additive manufacturing using water atomized steel powders, Met. Powder Rep. 72 (2) (2017) 111–117, https://doi.org/10.1016/j.mprp.2017.01.004.
[32] X. Lou, P.L. Andresen, R.B. Rebak, Oxide inclusions in laser additive manufactured stainless steel and their effects on impact toughness and stress corrosion cracking behavior, J. Nucl. Mater. 499 (2018) 182–190, https://doi.org/10.1016/j.jnucmat.2017.11.036.
[33] T. Zhou, H. Yu, S. Wang, Effect of microstructural types on toughness and microstructural optimization of ultra-heavy steel plate: EBSD analysis and microscopic fracture mechanism, Mater. Sci. Eng. A. 658 (2016) 150–158, https://doi.org/10.1016/j.msea.2016.02.001.
[34] Y. Wang, J. Hua, M. Kong, Y.i. Zeng, J. Liu, Z. Liu, Quantitative analysis of martensite and bainite microstructures using electron backscatter diffraction, Microsc. Res. Tech. 79 (9) (2016) 814–819, https://doi.org/10.1002/jemt.v79.910.1002/jemt.22703.
[35] M.-S. Baek, K.-S. Kim, T.-W. Park, J. Ham, K.-A. Lee, Quantitative phase analysis of martensite-bainite steel using EBSD and its microstructure, tensile and high-cycle fatigue behaviors, Mater. Sci. Eng. A. 785 (2020) 139375, https://doi.org/10.1016/j.msea.2020.139375.